RESEARCH ARTICLE

ESPL WILEY

Predicting monthly to multi-annual foredune growth at a narrow beach

Gerben Ruessink[1] | Geert Sterk[1] | Yvonne Smit[1,2] | Winnie De Winter[1,3] | Pam Hage[1,4] | Jasper J. A. Donker[1,5] | Sebastiaan M. Arens[6]

[1]Department of Physical Geography, Faculty of Geosciences, Utrecht University, Utrecht, The Netherlands
[2]QuSoft, University of Amsterdam, Amsterdam, The Netherlands
[3]Stichting De Noordzee, Utrecht, The Netherlands
[4]TAUW Nederland, Capelle aan den IJssel, The Netherlands
[5]Geodan, 's-Hertogenbosch, The Netherlands
[6]Arens Bureau for Beach and Dune Research, Soest, The Netherlands

Correspondence
Gerben Ruessink, Department of Physical Geography, Faculty of Geosciences, Utrecht University, PO Box 80.115, 3508 TC Utrecht, The Netherlands.
Email: b.g.ruessink@uu.nl

Funding information
Stichting voor de Technische Wetenschappen, Grant/Award Number: 13709

Abstract

An open-source quantitative model for predicting coastal foredune growth at monthly to multi-annual (meso)temporal scales is developed. The model builds on the established fetch framework as a surrogate for the complex micro-scale aeolian processes on the beach, to which rain and groundwater-induced spatiotemporal surface moisture dynamics are added as factors limiting aeolian sand supply to foredunes. The model shows great skill in an application at Egmond aan Zee, The Netherlands, with a predicted growth of 16.5 m^3/m/yr comparing favourably to the observed growth of 17.3 m^3/m/yr. Rain, surface moisture dynamics as well as beach width reduction by storm-induced elevated sea levels are shown to be important factors that jointly reduce meso-scale sand supply below the potential (i.e., unlimited) maximum, in our case study by almost 5 m^3/m/yr. These factors are most relevant for strong (here, above 15.5 m/s) onshore winds. Consistent with expectations from the literature, meso-scale foredune growth results primarily from moderately strong (9.5–12.5 m/s) shore-oblique winds, which are frequent and do not result in supply-limited conditions. At the study site these winds are most common in winter and hence foredune growth is predicted to vary seasonally, consistent with the observations. Because of the promising results we believe that our model has potential for quantifying how quickly a foredune can recover after an episodic erosion event because of storm waves.

KEYWORDS
aeolian transport predictions, fetch, surface moisture, beach–dune interaction, coastal dune evolution

1 | INTRODUCTION

Sandy beaches and their adjoining dunes are present on all continents on Earth and form approximately 30% of the world's ice-free shorelines (Luijendijk et al., 2018). In addition to being inherently important landform units of sandy coasts, coastal dunes offer numerous important ecosystem services to humankind, including coastal protection, provision of habitat for many plant and animal species, tourism and water purification (Barbier et al., 2011; Everard et al., 2010). Coastal protection is arguably the most valuable service when dunes are adjacent to large populations; accordingly, the episodic erosion of the most seaward dune (foredune) because of storm wave processes has

been studied extensively (Castelle et al., 2015; Davidson et al., 2020; De Winter et al., 2015; Van Thiel de Vries et al., 2008). This has resulted in well-developed foredune erosion models for use in scientific and applied studies (De Winter & Ruessink, 2017; Roelvink et al., 2009; Van Gent et al., 2008). The increasing risk of dune erosion under global change and the associated loss of valuable services has accelerated research on the capacity of foredunes to recover towards their pre-storm condition (Bullard et al., 2019; Castelle et al., 2017; Cohn et al., 2019; Morton et al., 1994). The timescale on which foredunes rebuild from sand delivered by the wind from the adjacent beach is remarkably longer (typically years) than that of wave-induced foredune erosion (hours–day). Foredune recovery is thus due to

numerous wind events with different magnitude and frequency. The scale gap between complex small-scale (seconds–hours) aeolian processes on the beach (Ellis & Sherman, 2013) to longer term (seasons–years; often termed meso-scale) foredune growth is one of the major obstacles in predicting foredune growth (Bauer & Davidson-Arnott, 2003; Delgado-Fernandez, 2011; Houser & Ellis, 2013; Sherman, 1995; Walker et al., 2017).

Meso-scale sand supply to foredunes is often modelled with drift potentials (Keijsers et al., 2014; Strypsteen et al., 2019; De Vries et al., 2012). An equilibrium aeolian transport equation is forced with time series of wind data from a regionally representative meteorological station and the resulting instantaneous transport rates are time-integrated to yield the potential meso-scale supply. This approach works reasonably well on wide (>200 m) beaches (Keijsers et al., 2014; Strypsteen et al., 2019), but overestimates observed foredune growth along more narrow beaches substantially (Davidson-Arnott, 1990; Delgado-Fernandez, 2011; De Winter et al., 2020; Sarre, 1989). Parameters in the transport equation can be tuned to minimize the data model discrepancies (Duarte-Campos et al., 2018; Hallin et al., 2019; Yokobori et al., 2020) but case-specific calibration limits real predictive value and likely hides sources of model error. The dependence of meso-scale sand supply on beach width is related to the fetch effect: the saltation cascade-induced increase in the transport rate with distance downwind from the leading edge of an erodible bed until equilibrium transport is reached (Bauer & Davidson-Arnott, 2003; Delgado-Fernandez, 2010; Gillette et al., 1996; Shao & Raupach, 1992). The distance required to achieve maximum transport, termed the critical fetch, ranges from only a few metres when the wind speed is just above the threshold of motion (Jackson & Cooper, 1999) to over 150 m in much stronger winds (Bauer et al., 2009; Davidson-Arnott et al., 2008). Water films adsorbed to the sand grains impede the saltation cascade and the critical fetch may thus be greater over damp surfaces (Davidson-Arnott & Dawson, 2001; Davidson-Arnott et al., 2008). Moreover, when the sand becomes too wet (typically when the moisture content exceeds 10% by weight), grain entrainment by the wind is halted completely, and this thus reduces the source width of the beach. A critical fetch distance of tens of metres or more can thus easily exceed the effective beach width. Consequently, the transport at the beach–dune transition will not have reached its maximum value, and not accounting for fetch-induced supply limitations will bias high meso-scale supply predictions. Strong onshore winds are often considered the primary condition responsible for the largest supply limitations (Arens, 1997; Delgado-Fernandez & Davidson-Arnott, 2011; Davidson-Arnott, 1990). The drift potential under such conditions is large but the reduced beach width because of elevated ocean water levels in combination with a large critical fetch imply that the actual supply may be limited severely (Tuijman et al., 2020). Because of the numerous interacting factors influencing beach width and sand transport magnitude, there is still considerable ambiguity about which wind conditions are most significant in growing foredunes.

Bauer and Davidson-Arnott (2003) proposed to parametrize the fetch effect with a simple trigonometric function as a means to aggregate micro-scale aeolian sediment transport processes and hence to, first, facilitate the prediction of meso-scale sand supply to foredunes and, second, examine the factors that mediate and control this supply. Delgado-Fernandez (2011) translated Bauer and

Davidson-Arnott's (2003) theory into an operational framework for predictive purposes and showed improved skill in hindcasting foredune growth at Greenwich Dunes, Prince Edward Island National Park, Canada, compared to a hindcast based on drift potentials; see also Walker et al. (2017). While the improved predictions show the feasibility of the fetch approach, the assumption of a spatially invariant surface moisture content contrasts with the strong groundwater-induced zonation in beach surface moisture levels generally observed on beaches (Brakenhoff et al., 2019; Namikas et al., 2010; Pollock & Hummon, 1971; Schmutz & Namikas, 2018; Smit et al., 2019).

The main objective of this paper is to extend the established fetch framework for meso-scale sand supply to foredunes into a quantitative model by coupling groundwater-driven surface moisture dynamics to an aeolian module that predicts the increase in aeolian sand transport over a bed with spatially varying surface moisture content. The output of the module is a time series of instantaneous onshore sand transport rate at the beach–dune transition, which can be integrated with time and converted into foredune volume growth. The paper starts by describing the developed model, called Psamathe after the Greek goddess of sand beaches, which is followed by the analysis of a series of synthetic simulations to illustrate model behaviour as a function of wind speed and direction as well as tide- and surge-induced beach width variations. Psamathe is then applied to simulate foredune growth at Egmond aan Zee, The Netherlands, and compared to observed growth calculated from a 4-year dataset of 30 digital elevation models. Various scenario runs are analysed to examine the importance of beach width variations and moisture dynamics in controlling meso-scale sand supply. Also, the wind conditions most relevant to the observed foredune growth are examined. This paper ends with suggestions for further model development and with the main conclusions.

2 | METHODS

2.1 | Model description

Psamathe comprises three modules to compute the cross-shore and temporally varying water table elevation, surface moisture content and aeolian sand transport rate on a sandy beach. In brief, the water table module contains the one-dimensional nonlinear Boussinesq equation; the surface moisture module is based on the steady-state Van Genuchten (1980) soil water retention curve; and the aeolian module builds on the fetch-based models of Bauer and Davidson-Arnott (2003) and Delgado-Fernandez (2011). The three modules are run consecutively. The main inputs are a time-invariant cross-shore bed profile, a representative grain size and time series of forcing conditions, including wind speed and direction, rainfall and offshore wave parameters (height and period). The main output is a time series of the aeolian sand transport rate at the beach–dune transition, from which foredune growth is computed under the assumption that all sand crossing this transition is deposited on the foredune. The groundwater and surface moisture modules have previously been described in Brakenhoff et al. (2019), and the first version of the fetch model can be found in Hage et al. (2020). Since then, several new features have been introduced to improve the model's applicability (in part described in Tuijman et al., 2020), such as a different scheme to relate

surface moisture to the critical fetch, the effect of rain on aeolian sand transport, various equations to estimate the potential sand transport rate and a coupling to foredune volume growth by calculating the onshore in addition to the total aeolian transport rate at the beach–dune transition. In the following we describe the three modules in more detail, which consolidates all modifications made since the first model version was introduced (Hage et al., 2020). Finally, we note that the model was previously called Aeolus (Hage et al., 2020; Tuijman et al., 2020); to avoid confusion with other models called Aeolus (e.g., Di Cosmo et al., 2014) we have changed the name to Psamathe.

2.1.1 | Groundwater

Psamathe contains the nonlinear Boussinesq equation (Raubenheimer et al., 1999) with spatially constant aquifer thickness d [m], extended to include the infiltration of water into the beach face due to wave runup (Kang et al., 1994), to simulate cross-shore and temporal water table fluctuations $\eta(x,t)$:

$$\frac{\partial \eta(x,t)}{\partial t} = \frac{K}{n_e} \frac{\partial}{\partial x} \left\{ [d + \eta(x,t)] \frac{\partial \eta(x,t)}{\partial x} \right\} + \frac{U_l}{n_e}. \tag{1}$$

The unit of η is metres (with respect to mean sea level, MSL), x is cross-shore location [m], t is time [s], K is the hydraulic conductivity of the sand [m/s], n_e is the non-dimensional specific yield and U_l is the infiltration flow rate of wave runup on the beach per unit area [m/s], here included as proposed in Brakenhoff et al. (2019). Equation (1) assumes the sand to be homogeneous and isotropic, and the groundwater flow to be essentially horizontal. These are generally realistic assumptions for sandy beaches (Raubenheimer et al., 1999). Equation (1) is solved numerically with a centred finite difference method in space and a fourth-order Runge–Kutta integration technique in time. The seaward boundary condition is a moving shoreline at location $x_{sh}(t)$; the elevation at $x_{sh}(t), \eta_{sh}(t)$, is taken as the sum of the offshore ocean water level $\zeta_0(t)$ and the wave breaking-induced setup at the shoreline, $\xi_{sh}(t)$. We estimate $\xi_{sh}(t)$ using offshore wave data and the Stockdon et al. (2006) parametrization, their eq. (10). The imposed landward boundary condition is $\partial \eta / \partial x = 0$, which implies that there is no groundwater discharge to the beach beneath the foredune. The beach profile $z_b(x)$ [m MSL] must be monotonically increasing landward; in other words, Psamathe cannot handle sandbar–trough profiles.

2.1.2 | Surface moisture

Following the conceptual idea of Namikas et al. (2010), water table depth $h(x,t) = z_b(x) - \eta(x,t)$ [m] is related to gravimetric surface moisture content $w_s(x,t)$ [%] with a steady-state retention curve. Such a curve describes how gravimetric moisture content w changes with height above the water table under equilibrium; w_s is then the moisture content where the retention curve truncates the bed profile. Here, w_s is computed for each t and all x that are not submerged by the ocean tide using the Van Genuchten (1980) retention curve:

$$w_s(x,t) = w_{res} + \frac{w_{sat} - w_{res}}{\left\{ 1 + [\alpha h(x,t)]^n \right\}^{1-1/n}}, \tag{2}$$

where w_{res} and w_{sat} are the residual and saturated gravimetric water content [%], respectively. The parameter α [1/m] is related to the inverse of the air entry suction and determines the thickness of the capillary fringe. The non-dimensional parameter n determines the steepness of the retention curve when h exceeds the thickness of the capillary fringe and thus the range of h values over which w_s varies between w_{sat} and w_{res}. Typical α and n values for sand are 3.5/m and 3.2, respectively (Tuller & Or, 2005).

2.1.3 | Aeolian transport

Bauer and Davidson-Arnott (2003) proposed to parametrize the downwind increase in the aeolian transport rate q as the product of the (maximum) potential transport rate q_p and a trigonometric function, for which various forms were suggested. Based on agreement with observations on agricultural fields and a coastal beach, Delgado-Fernandez (2010) suggested that

$$q(F) = \min \left[q_p, q_p \sin \left(\frac{\pi}{2} \frac{F}{F_c} \right) \right] \tag{3}$$

was the most appropriate of these forms. In this equation, F is the distance downwind from the location where aeolian transport starts, and F_c is the critical fetch, which depends on wind speed U and w_s (Delgado-Fernandez, 2010, 2011). In Delgado-Fernandez (2011)'s implementation of Equation (3), U and w_s were taken as cross-shore constant and hence q could be computed simultaneously at all cross-shore locations. This approach is no longer valid here as the w_s predicted with Equation (2) varies in the cross-shore direction from w_{sat} near the shoreline to w_{res} on the dry beach. Therefore, Equation (3) is rewritten (Hage et al., 2020) into a spatially forward-stepping (i.e., from sea to land) equation:

$$q(i) = \begin{cases} \min \left[q_p, q(i_1 - 1) + q_p \sin \left(\frac{\pi}{2} \frac{F(i)}{F_c(i)} \right) \right] & \text{if } w_s(i) \leq w_{s,max} \\ 0 & \text{otherwise}. \end{cases} \tag{4}$$

Figure 1 provides a visual account of this approach. For each grid point with w_s less than a user-specified moisture threshold $w_{s,max}$ above which aeolian transport is inhibited (typically, $w_{s,max} = 10\%$; Figure 1a), the critical fetch is computed as in Delgado-Fernandez (2011) with

$$F_c(i) = p_F(w_s) \times (4.38U - 8.23) \tag{5}$$

(see Figure 1b). The rightmost term in this equation is the U dependence of the critical fetch for dry sand as proposed by Delgado-Fernandez (2011), who based it on the field results of Davidson-Arnott (1990). The term $p_F(w_s)$ describes the moisture-dependent increase in the dry-sand F_c. Here, as in Delgado-Fernandez (2011), a step function is adopted with $p_F = 1$ for $w_s < 4\%, p_F = 1.25$ for $4\% \leq w_s < 6\%$ and $p_F = 1.75$ for $6\% \leq w_s \leq 10\%$. In case a value of $w_{s,max}$ above 10% is chosen, the p_F for all $w_s > 10\%$ is 2.5. For each
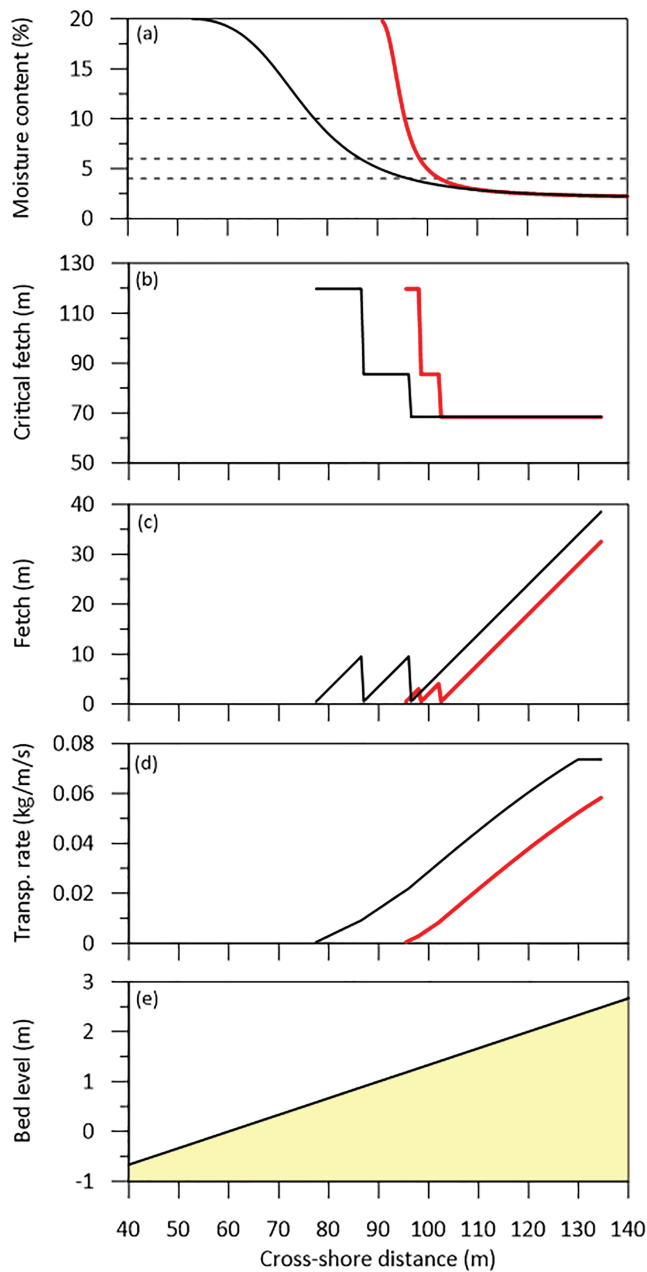
FIGURE 1 Example of fetch model: (a) surface moisture w_s; (b) critical fetch F_c; (c) fetch F; and (d) aeolian transport rate q (i.e., Equation 4) versus cross-shore distance x for a case when the aeolian transport at the beach–dune transition reaches the potential transport q_p (black line) and is limited (red line). The two situations are from the synthetic run in Figure 2 at high tide ($t = 0$; red line) and at 1.5 h after low tide ($t = 8.5$ h; black line). The speed U of the shore-normal wind is 17.5 m/s in both situations, resulting in $q_p = 0.0734$ kg/m/s with Kok *et al.* (2012), $D = 250$ μm and default values. The dashed lines in (a) are moisture values of 10%, 6% and 4%, respectively. The computation of F_c starts when w_s drops below $w_{s,max} = 10\%$. The steps in (b) illustrate the moisture effect on F_c (Equation 5. Part (e) shows the bed profile, for reference. The beach–dune transition is at bed level $z_{bdt} = 2.5$ m ($x = 135$ m) [Color figure can be viewed at wileyonlinelibrary.com]

group of grid points with equal F_c, indicated in Equations (4) and (5) by the list i of spatial indices (generally, $i = 1$ corresponds to the locations with $6\% \leq w_s \leq 10\%$, $i = 2$ to $4\% \leq w_s < 6\%$ and $i = 3$ to $w_s < 4\%$), the fetch F is computed as the distance downwind of the last grid location in the upwind (seaward) F_c group. This is indicated in

Equation (4) by $i_1 - 1$, with i_1 the first location index of the ith F_c group. In case F exceeds $F_c(i)$, F is set equal to $F_c(i)$, implying that the sin term in Equation (4) equals 1. The present F computation implies that, in contrast to its use in Equation (3), F does not increase with x across the entire beach but is reset to 0 each time F_c changes (Figure 1c). In essence, Equation (3) implies that the transport rate in a group of grid points with constant F_c thus equals the upwind supply ($= q(i_1 - 1)$ in Equation (4)) increased with the fetch-based supply within the group ($= +q_p \sin\{(\pi/2)[F(i)/F_c(i)]\}$ in Equation (4)) up to a maximum of q_p. In the case where F_c is constant for all grid locations, Equation (4) reduces to Equation (3). Consistent with field observations (Davidson-Arnott & Dawson, 2001), the example cases show that q first increases relatively gently with x (caused by the high F_c), then more steeply to become constant if q_p is reached (Figure 1d). The computation of q is continued up to and including the beach–dune transition with the user-specified elevation z_{bdt}. The q at its transition is coined q_{bdt}; its onshore component, $q_{bdt,on}$, is

$$q_{bdt,on} = q_{bdt} \cos\theta_{SN}, \qquad (6)$$

in which θ_{SN} is the wind direction with respect to the shore-normal direction. For $|\theta_{SN}| > 90°$, q_p and hence q_{bdt} are set to 0. Under the assumption that all sediment that crosses the beach–dune transition is deposited on the foredune, the volume growth of the foredune ΔV during a given time interval can be computed as

$$\Delta V = \frac{\sum \left(q_{bdt,on}(t)\Delta t\right)}{(1-p)\rho_s}. \qquad (7)$$

Here, Δt is the model output time step [s], p is bed porosity (typically, 0.4) and ρ_s is the sediment density [kg/m³] (for quartz sand, $\rho_s = 2650$ kg/m³).

In Psamathe the potential sand transport rate q_p [kg/m/s] in Equation (4) can be computed with three different equations. The default model is that of Kok et al. (2012), which was also proposed in Durán et al. (2011) and reads

$$q_p = C_{DK}\frac{\rho_a}{g}U_{*t}\left(U_*^2 - U_{*t}^2\right). \qquad (8)$$

The constant $C_{DK} = 5$, ρ_a is the density of air [kg/m³] (for air with a temperature of 10°C, $\rho_a = 1.25$ kg/m³), U_* [m/s] is the shear velocity and U_{*t} is the saltation threshold shear velocity. In Psamathe, U_* is linked to U assuming a logarithmic velocity profile as $U_* = aU$ (Hsu, 1974) with

$$a = \frac{\kappa}{\log\left(\frac{z}{z_0}\right)}. \qquad (9)$$

The parameter $\kappa = 0.41$ is Von Karman's constant, z is the height above the bed [m] where U is measured and z_0 is the roughness length [m]. Based on vertical profiles of U measured at several beaches, Hsu (1974) rounded a to 0.04 for z between 2 and 10 m. For U_{*t} the saltation fluid threshold velocity proposed by Shao and Lu (2000) was taken, modified to include the bed slope (β) effect on the initiation of motion:

$$U_{*t} = \Phi(\beta) A_N \sqrt{\frac{\rho_s - \rho_a}{\rho_a} gD + \frac{\gamma}{\rho_a D}}. \tag{10}$$

The non-dimensional parameter A_N is 0.111, γ is 2.9×10^{-4} N/m (Kok et al., 2012) and $\Phi(\beta)$ is given as (Iversen & Rasmussen, 1994)

$$\Phi(\beta) = \sqrt{\cos\beta + \frac{\sin\beta}{\tan\Psi}}, \tag{11}$$

with $\Psi \sim 33°$ the angle of repose. The alternative q_p formulations embedded in Psamathe are those of Hsu (1971) and Lettau and Lettau (1978), which read

$$q_p = 0.1 \times [-0.47 + 4.97 D_{mm}] \times 10^{-4} \left(\frac{U_*}{\sqrt{gD}}\right)^3 \tag{12}$$

and

$$q_p = C_L \sqrt{\frac{D}{D_{250}} \frac{\rho_a}{g}} U_*^2 (U_* - U_{*t}), \tag{13}$$

respectively. The term $[-0.47 + 4.97 D_{mm}] \times 10^{-4}$ in Equation (12) represents the aeolian sand transport coefficient K_a with units g/cm/s and contains the dependence of the potential transport rate on the grain size D. It was formulated empirically based on laboratory and field data available at the time. Note the grain size has to be specified in millimetres (hence, D_{mm}). The term between the large brackets in Equation (12) is a Froude number, where $g = 9.81$ m/s^2 is gravitational acceleration. In Equation (13) $D_{250} = 250 \times 10^{-6}$ m and $C_L = 6.7$. Finally, it is noted that the Hsu (1971) equation does not contain a threshold for motion. Psamathe, however, sets q_p to 0 if U_* is less than U_{*t}.

Psamathe includes the effect of rain on aeolian sand transport, similar to an earlier modelling study (Van Dijk et al., 1999), following the inferences of Arens (1996) based on extensive field data collected under dry and rainy conditions. First, if it rains, U_{*t} is raised by 35% irrespective of the rain intensity I_r. Thus, rain results in $q_p = 0$ for all wind conditions with $U_* \leq 1.35 U_{*t}$. For stronger winds, q_p reduces with Kok et al. (2012) and Lettau and Lettau (1978) but remains unaffected with Hsu (1971). Second, if I_r exceeds 2 mm/h, q_{bdt} is set to 0. The beach is then assumed to be too wet to result in aeolian sand transport.

2.1.4 | Synthetic runs

We now illustrate the general characteristics of Psamathe with a series of synthetic simulations. The first (default) case comprises a 1:30 linear sloping beach subject to a vertical (ocean) tide with a 12 h period and a 2 m range, with no waves (runup) and rain. The aeolian transport module was subsequently run for wind speeds U between 10 and 25 m/s with a step size of 0.25 m/s; for each wind speed, the wind direction θ_{SN} was varied from 0° to 89° with a 1° step size. The second and third cases equal the first case but with a 1 m and 3 m tidal range, respectively. The fourth and final case has a 1:30 sloping beach profile, and is subject to a storm surge on top of the 12 h tide with a 2 m range; the aeolian module in this case was run only with a shore-normal wind with a speed of 17.5 m/s. The surge is schematized as a

Gaussian (in time) change in sea level, with a maximum super-elevation of 2 m coinciding with a high tide (i.e., the total water level at high tide is 3 m) and a half-width (in time) of 12 h. In all four cases, the parameters in the groundwater module were set to values also adopted in the Egmond case ($K = 40$ m/day, $n_e = 0.3, d = 15$ m; Section 6), while those in the surface moisture module are typical sand values ($w_{res} = 2\%, w_{sat} = 20\%, \alpha = 3.5$ and $n = 3.2$). For q_p the Kok et al. (2012) model was chosen, with $a = 0.04$ to relate U to U_*. Because of the chosen wind speeds, the saltation threshold velocity was always exceeded. As in the Egmond case, the threshold moisture content $w_{s,max}$ was taken as 10% and the dune line was set to $z_{bdt} = 2.5$ m. The first three cases were run for 40 tidal cycles (20 days) to allow for a sufficient spin-up of the model, with the results presented below taken from the final cycle. The fourth surge case was run for 50 tidal cycles, with the maximum surge level coinciding with the high tide of the 40th tidal cycle.

As can be seen for the default case in Figure 2a, the groundwater depth in the intertidal zone starts to increase immediately after high tide ($t = 0$ h). Rather than reaching maximum values at low tide ($t = 6$ h), the groundwater depth continues to increase until the beach is inundated by the rising tide. This is best visible in Figure 2a for $t = 8.5 - 11$ h. For most of the intertidal zone the groundwater remains close to the beach surface, with typical depths of 0.3 m or less. Landward of the high-tide position ($x > 90$ m) groundwater depth generally exceeds 0.5 m or more and temporal variability in depth is small. In more detail, the groundwater fluctuations increasingly lag behind the ocean tide in the landward direction. For example, around $x = 100$ m and 120 m the groundwater depth is lowest (i.e., high tide in groundwater) about 1 h and 2.5 h after ocean high tide,
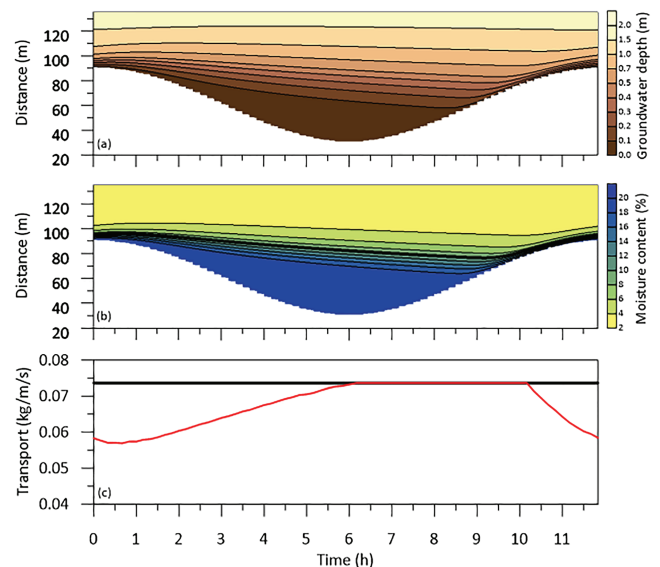
FIGURE 2 Results of default synthetic simulation: (a) spatiotemporal variability in groundwater depth h and (b) surface moisture content w_s during a tidal cycle in the default synthetic simulation (case 1). The thick black contour in (b) is $w_{s,max} = 10\%$. Part (c) shows the aeolian transport rate at the dune line (q_{bdt}; red line) and the potential rate (q_p; black line) versus time for a shore-normal wind with a speed of 17.5 m/s. The beach–dune transition is at bed level $z_{bdt} = 2.5$ m ($x = 135$ m). The white areas in (a) and (b) are inundated by the ocean tide. The two examples in Figure 1 were taken from this simulation at $t = 0$ (red line) and $t = 8.5$ h (black line) [Color figure can be viewed at wileyonlinelibrary.com]

respectively. In the default case, large parts of the intertidal beach have a surface moisture content that exceeds $w_{s,max} = 10\%$ (Figure 2b). The maximum fetch (i.e., the cross-shore distance between the 10% moisture contour and the dune line) is not largest during low tide, when the beach is widest, but several hours (≈ 3 h in the default case) later because of the ongoing increase in groundwater depth and hence drying of the beach after low tide. Figure 2b thus clearly indicates that the instantaneous shoreline is not a good proxy of the location where aeolian transport may start, neither spatially nor temporally. For a shore-normal wind with $U = 17.5$ m/s the aeolian transport rate is predicted to reach q_p for approximately 4 h during this tidal cycle, from low tide to 4 h later (Figure 2c). During all other parts of the tidal cycle, including the entire falling stage ($t = 0 - 6$ h), the transport at the dune line is predicted to be limited ($q_{bdt} < q_p$). The lowest q_{bdt} ($q_{bdt}/q_p = 0.77$) is not predicted for the moment of high tide but about 0.5 h later. This reflects the temporal lag of the groundwater high tide, and hence wetting of the sand, in the dry beach.

To further examine under which wind speeds and directions the transport is predicted to be limited during at least part of the tidal cycle, the ratio of tide-integrated predicted to potential transport at the dune line was computed for all simulations in the three tide-only cases. If this ratio is less than 1, then q_{bdt} did not reach q_p during the entire tidal cycle; for the simulation shown in Figure 2 ($U = 17.5$ m/s, $\theta_{SN} = 0°$ and tidal range $= 2$ m), for example, this ratio was about 0.9. Figure 3a shows that limited transport in case 1 (tidal range $= 2$ m) is predicted for shore-normal winds exceeding about 13 m/s and for an increasing range of angles with increasing U. These results reflect the increase in critical fetch F_c with U (i.e., Equation 5) and the increase in available fetch for more oblique winds. The main effect of a change in tidal range is to reduce the width of the dry beach (z_{bdt} was constant in the three tide-only runs). This is reflected in a substantially smaller and larger part of (U, θ_{SN}) space with limited transport for the case with a 1 m (Figure 3b) and 3 m (Figure 3c) range, respectively, compared to the default case. Obviously, the maximum beach width (during low tide) is largest in the 3 m case, but since most of the intertidal beach remains wetter than the moisture threshold, this increase in beach width does not compensate for the reduction in the width of the dry beach.

Figure 4 presents the results of the surge run (case 4). Even though the surge itself is symmetric with time around the high tide at $t = 0$, the response of the groundwater depth and hence surface moisture and aeolian transport at the dune line is not. It is obvious that the beach fills more rapidly during the rising part of the surge ($t < 0$) than it drains afterwards (Figure 4a); for example, even 72 h after the peak in surge level, the groundwater near the dune line ($x = 135$ m) has not fallen back to its pre-surge level. During the peak in surge level, the total water level exceeds the elevation of the dune line (Figure 4a)

and hence the aeolian transport equals 0 for several hours around $t = 0$ (Figure 4c). Because of the slow drop in groundwater depth, most of the beach above the normal high-tide level ($x > 90$ m) remains so wet for at least 48 h (Figure 4b) that the aeolian transport at the dune line (with a shore-normal wind with speed $U = 17.5$ m/s) does not reach its potential value (Figure 4c). Figure 4 thus clearly demonstrates that a surge does not only shut down the aeolian system during peak water level but can also limit aeolian transport on the following days because of increased moisture levels, even though the surge in ocean water level has already disappeared.

2.2 | Case study Egmond aan Zee, The Netherlands

2.2.1 | Geographic setting

The study site is located about 3 km south of the town of Egmond aan Zee (Figure 5) along the approximately north–south oriented Holland coast of the Netherlands. It is a multi-barred, wave-dominated,
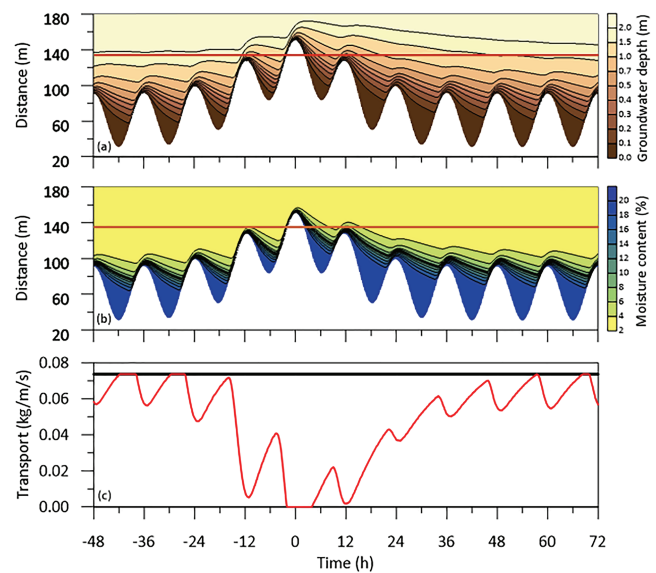
FIGURE 4 Results of surge simulation: (a) spatiotemporal variability in groundwater depth h and (b) surface moisture content w_s during 10 tidal cycles in the synthetic surge simulation (case 4). The surge is symmetric with time and peaks at $t = 0$. Part (c) shows the aeolian transport rate at the dune line (q_{bdt}; red line) and the potential rate (q_p; black line) versus time for a shore-normal wind with a speed of 17.5 m/s. The beach–dune transition, indicated by the horizontal brick-red line in (a) and (b), is at bed level $z_{bdt} = 2.5$ m ($x = 135$ m). The thick black contour in (b) is $w_{s,max} = 10\%$. The white areas in (a) and (b) are inundated by the ocean tide [Color figure can be viewed at wileyonlinelibrary.com]
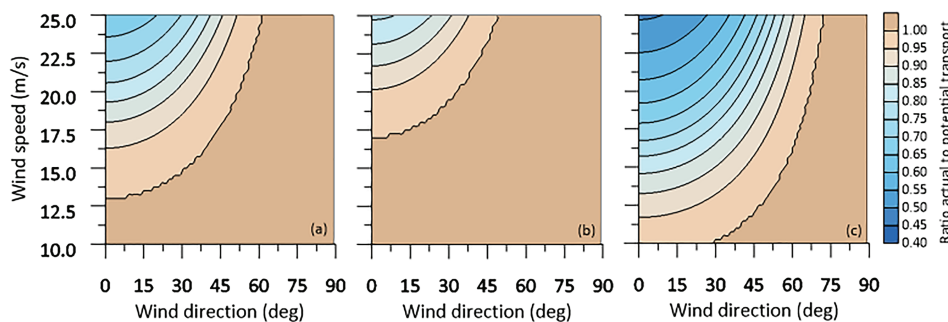
FIGURE 3 Ratio of tide-integrated predicted to potential transport at the dune line, q_{bdt}/q_p, as a function of wind speed U and wind direction θ_{SN} for the synthetic simulations with a tidal range of (a) 2 m, case 1; (b) 1 m, case 2; and (c) 3 m, case 3 [Color figure can be viewed at wileyonlinelibrary.com]

FIGURE 5 Location of study site. The beach poles form an alongshore reference line, with the km number referring to the distance to the zero point at the northern end of the Holland coast [Color figure can be viewed at wileyonlinelibrary. com]
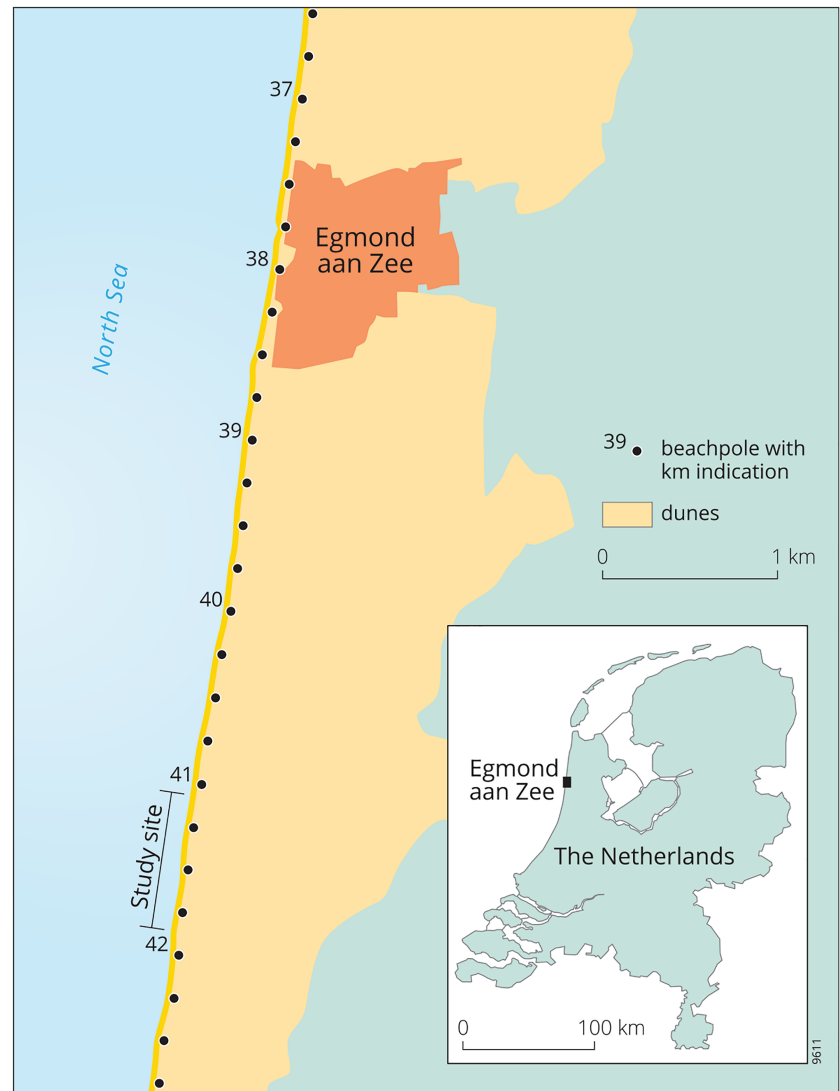
microtidal (≈ 1.5 m range) environment with a moderately sloping (1:30–1:50), fine–medium sand ($D \sim 250$ μm) intertidal beach and a 20–25 m high established foredune. Winds, waves and surges vary seasonally (Wijnberg, 2002), with the most energetic conditions in the winter months November–February. Especially during strong winds from the northwest (>20 m/s), offshore significant wave heights can reach 5–7 m and surge levels can exceed 1 m. Such conditions often result in substantial foredune scarping and slope failure by means of rotational slumps (De Winter et al., 2015), which can extend to a height of 14–17 m above mean sea level. This upper erosion limit marks a striking change in foredune slope, where the steep (1:2.5) erosional front face of the foredune turns into a much more gentle slope toward the crest. This upper part of the foredune is covered densely in European marram grass (*Ammophila arenaria*) (Schwarz et al., 2021). Large-scale (km) alongshore variability in foredune height and shape is small. Despite the seasonal cycles in forcing, the intertidal beach exhibits only minor seasonal variations in width and volume (Quartel et al., 2008). During prolonged (several years) periods without notable storm surges, wind-blown sand accumulates at the base of the steep foredune face, and initially isolated embryo dunes can develop and grow into an alongshore continuous incipient foredune ridge (De Winter et al., 2015; Ruessink et al., 2019). Wind-blown sand transport across the abrupt change in slope and the foredune crest is

generally small to negligible (De Vries et al., 2012; Ruessink et al., 2018; Schwarz et al., 2021).

2.2.2 | Morphological change and forcing conditions

Beach–dune topography has been measured at Egmond with a monthly to seasonal interval since December 2013, in concert with high-frequency time series of wind, rainfall, water level and wave characteristics. Details of data acquisition and processing are provided in a data descriptor paper (Ruessink et al., 2019) and are therefore not reiterated here. For this study, we focus on an 800 m stretch of coast where an incipient foredune ridge developed after the dune erosion event of 21 and 22 October 2014. Thirty digital elevation models (DEMs) with a 1×1 m resolution have been available since: the first on 15 March 2015 and the last on 7 January 2019. They all cover the region from the mid- to high-tide level to the location where the foredune changes abruptly in slope. During the selected period the wind speed U measured at 10 m height at the IJmuiden WMO 06225 meteorological station (Ruessink et al., 2019) varied between 0 and 29.4 m/s (Figure 6b), and showed a clear seasonal variation (Figure 6c). The dominant wind direction was southwest. Rain

intensity data (not shown in Figure 6) were collected at the nearby Wijk aan Zee WMO 06257 station. Both WMO stations are operated by the Royal Netherlands Meteorological Institute (KNMI).

As proposed in Cohn et al. (2018), the linear sum of the offshore water level $\zeta_0(t)$ and the 2% runup exceedance value (here based on the Stockdon et al., 2006, parametrization) can be used to elucidate which part of the profile has been subject to predominantly wind or wave (or both) processes; in other words, to determine the elevation of the beach–dune transition, z_{bdt}. Cohn et al. (2018) assumed that all morphological change in regions influenced by this total water level (TWL) more than 2% in time were wave induced. In this study, the 2% exceedance value of TWL was about 1.8 m, with a clear seasonal variation from about 2.0 m in winter to less than 1.4 m in summer (Figure 6e). The offshore water level and wave data used to compute the TWL were collected at the 'IJmuiden buitenhaven' tidal station and the 'IJmuiden munitiestortplaats' wave buoy, respectively (Ruessink et al., 2019). All volume changes above the maximum TWL are clearly wind induced, and changes between the 2% and maximum value are potentially affected by both wind and waves. The maximum TWL was encountered near the end of the study period (December 2018; Figure 6d) and was estimated at ≈ 3.0 m. Maximum TWL values in summer were 2.0 m or less, and between 2.5 and 3.0 m in the other parts of the year (Figure 6e). Based on these TWL statistics, we take the 2.5 m contour as the elevation of the beach–dune transition. This value is above all monthly 2% exceedance values and all maximum values in summer, and equal to or slightly below all maximum winter values. Furthermore, our interpretation of DEMs of difference, in concert with orthophotos (Ruessink et al., 2019) and observations in the field, highlight that the seaward base of the embryo dune ridge is near 2.5 m, implying that wind-blown sand was deposited below the maximum TWL.

The alongshore median volume gain on the seaward side of the foredune (i.e., between the 2.5 m contour and the location of the change in slope) was about 69 m³/m between March 2015 and January 2019 (Figure 6a). The interquartile range (middle 50%) in this

gain was about 10 m³/m, indicating that alongshore variability in aeolian sand deposition was small. Consistent with an earlier study for the Dutch coast (De Vries et al., 2012), the volume increase was fairly linear with time, although there were obviously moments when the increase was faster (e.g., October–December in 2016 and 2018) than during other moments (Figure 6a). The slope of the best-fit linear line was 17.3 m³/m/yr ($r^2 = 0.99$). The slopes through the temporal evolution of the alongshore 25% and 75% volume gain values were 16.2 and 18.4 m³/m/yr, respectively, again highlighting the only small alongshore variability in sand deposition in the 800 m wide study site.

2.2.3 | Model setup and scenarios

The bed profile used in the simulations was constructed from an annual database of surveys covering the foredune, the upper and intertidal beach as well as the subtidal zone with a 250 m alongshore spacing (Ruessink et al., 2019). In more detail, the bed profile applied was the time and alongshore average of all profiles collected in 2015, 2016, 2017 and 2018 in cross-shore lines 41.25, 41.50 and 41.75 (see Figure 5), which are all in the 800 m alongshore study site. Because the time- and alongshore-averaged profile still contained a small intertidal bar feature, it was subsequently smoothed with a quadratic loess interpolator (Plant et al., 2002) with a scale factor of 30 m. The smoothed profile commenced at $x = 0$ m with an elevation z of -2.57 m MSL, which is lower than any η_{sh} in the study period. All z above 6 m MSL were clipped to 6 m (from $x = 298$ m), and the profile ended at $x = 350$ m, where we expected tide-induced temporal variations in groundwater level to be essentially non-existent. The slope in the intertidal zone, between -1 and $+1$ m MSL, was about 1:50.

The settings of the groundwater module were taken from earlier modelling work for the study site (Hage et al., 2020; Smit, 2019): $K = 40$ m/day, $n_e = 0.3, C_l = 0.5$ and $d = 15$ m. The cross-shore grid spacing and the time step were set to 0.5 m and 2 s, respectively, with cross-shore profiles of water table fluctuations $\eta'(x)$ written as output
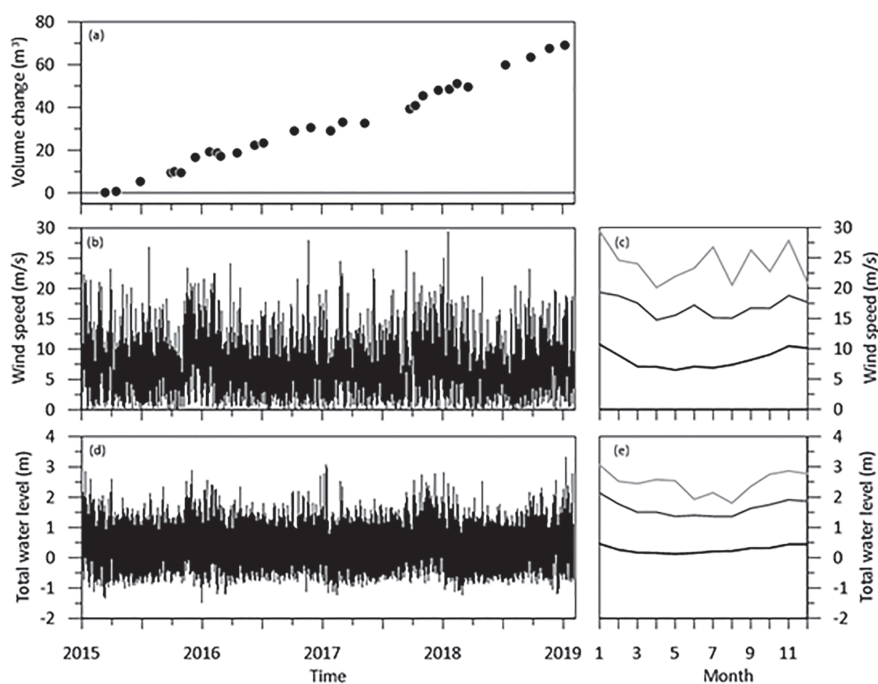
FIGURE 6 Time series of (a) volume change on the foredune, (b) wind speed, (c) monthly speed of winds with an onshore direction, (d) total water level and (e) monthly total water level. The volume change is in (a) the alongshore median value of the 800 m wide study region; all values are with respect to the first survey in March 2015. The three lines in (c) and (e) are (from dark to light grey) the median, 2% exceedance (i.e., the 98% percentile) and the maximum values

every 10 min ($\Delta t = 600$ s). In the surface moisture module, $w_{res} = 2.92\%, w_{sat} = 20.51\%, \alpha = 3.59$/m and $n = 3.69$ were adopted, based on Smit et al. (2019). The groundwater–surface moisture modules were run from 23 December 2014 until 8 January 2019. This encompasses the entire period for which topographic survey data were available (15 March 2015–7 January 2019) as well as the period 7 January 2014–15 March 2014, which is additionally used in the analyses that require a precisely 4-year-long prediction period (Section 6). The period prior to 7 January 2014 served as model spin-up time. The wind forcing for the aeolian transport model comprised the wind data measured at the IJmuiden WMO meteorological station modified to Egmond beach in order to account for the topographic effects (Bauer et al., 2012; Walker et al., 2017) of the high and steep foredune on the regional wind speed and direction. These modifications, derived from an extensive wind dataset at Egmond beach (De Winter et al., 2020; Tuijman et al., 2020) collected simultaneously with IJmuiden wind data, comprised a wind-direction-dependent reduction in wind speed, from about 0.7 (i.e., ratio of Egmond to IJmuiden wind speed) for shore-normal winds to 1 (i.e., no reduction) for alongshore winds (Tuijman et al., 2020, their fig. 6a). The wind direction on the beach equalled that at IJmuiden (De Winter et al., 2020) and the IJmuiden θ_{SN} was thus used in the computation of the available fetch; in contrast, winds at the beach–dune transition were observed to be deflected alongshore, with a maximum deflection angle of about 10–15° when the regional wind approach angle was 45° with respect to the shore normal (Tuijman et al., 2020, their fig. 6b). This deflected angle was used in the computation of the onshore component of the aeolian transport rate, Equation (6). For further details, we refer to De Winter et al. (2020) and Tuijman et al. (2020). The roughness length z_0 was set to 1×10^{-4} m based on the analysis of a large dataset of vertical wind profiles collected in autumn 2017 near the high-tide line on Egmond beach (Tuijman et al., 2020). With $z = 10$ m (the U measurement height at IJmuiden) and $\kappa = 0.41$, this implies $U_* = 0.0356U$. To compute dune volume growth $\Delta V, p = 0.4$ and $\rho_s = 2650$ kg/m³ were adopted. The ΔV computed with $q_{bdt,on}$ will henceforth be referred to as the supply-limited volume growth, ΔV_{lim}, to reflect that supply limitations were included in its prediction. The ΔV based on the onshore component of the potential transport rate, $q_{p,on}$ will be called the unlimited growth, ΔV_{unlim}.

Table 1 gives an overview of all model simulations. The reference run (termed Ref) is the Psamathe simulation with all model-embedded factors that affect meso-scale aeolian sand supply from the beach enabled. With a series of five additional simulations (Sc1–Sc5 in Table 1) the relative influence of rain, surface moisture, beach width variations because of storm surges, and topographic effects of the

foredune on the regional wind characteristics in regulating meso-scale aeolian sand transport and foredune growth are examined. In Sc1, $l_r = 0$ mm/h at all time steps (no rain); in Sc2, $w_s = 0\%$ at all non-submerged cross-shore locations, implying that aeolian transport commenced immediately at the (time-varying) shoreline position and that the critical fetch was a function of wind speed only; in Sc3, the groundwater module was forced (on the seaward side) with astronomical predicted tidal water levels (i.e., no storm surges) and without wave effects (no setup and no infiltration); in Sc4, the Sc3 forcing was also applied but the sand landward of the shoreline was assumed to be dry (as in Sc2); and in Sc5, the regional wind speed and direction were used without correction. The final two simulations (Sc6 and Sc7) equal the reference simulation but examine the sensitivity of the predicted foredune growth to the potential transport equation.

3 | RESULTS

3.1 | Reference run

Psamathe predicted non-zero onshore potential transport, $q_{p,on}$, during 18.6% of time in the examined period and a total unlimited dune volume gain ΔV_{unlim} of 73.8 m³/m (Figure 7a; Table 2), corresponding
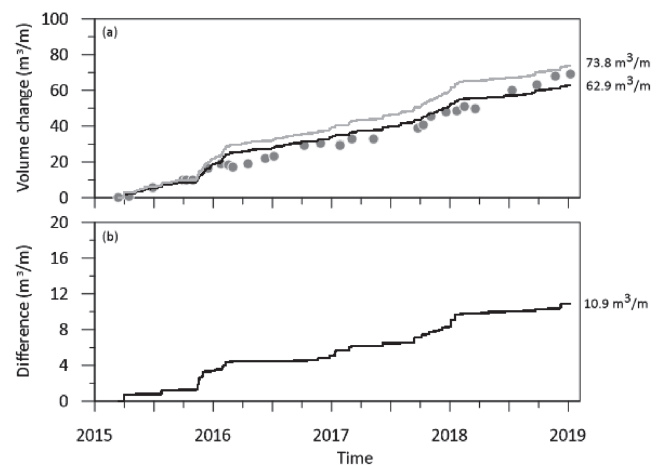
FIGURE 7 Time series of cumulative (a) unlimited (grey line) and limited (black line) volume change ΔV on the foredune and (b) difference between unlimited and supply-limited volume change. Both predicted ΔV in (a) include the effect of rain on the threshold of motion. The grey dots in part (a) are the observed cumulative volume changes. The numbers at the right vertical axes are the cumulative values at the end of study period
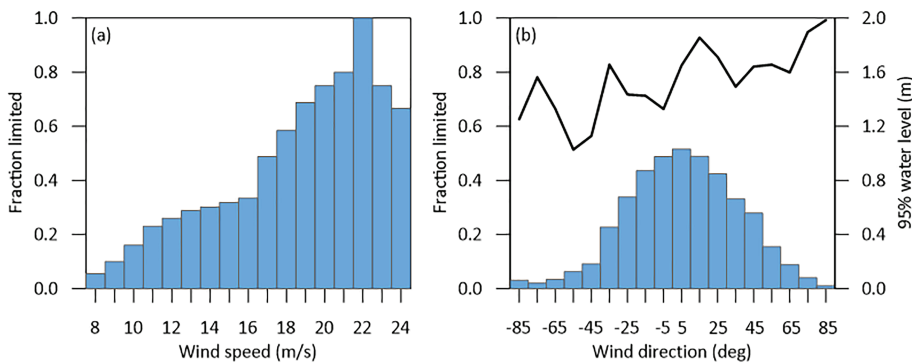
TABLE 1 Overview of model runs

Run name	Rain	Moisture	Surge	Wind correction	Remark
Ref	✓	✓	✓	✓	Kok et al. (2012)
Sc1		✓	✓	✓	
Sc2	✓			✓	
Sc3	✓	✓		✓	Astronomical tide, no waves
Sc4	✓			✓	= Sc3 without surface moisture
Sc5	✓	✓	✓		
Sc6	✓	✓	✓	✓	Hsu (1971)
Sc7	✓	✓	✓	✓	Lettau and Lettau (1978)

TABLE 2 Model results for foredune volume growth

Run name	Total ΔV_{lim} (m³/m)	Total ΔV_{unlim} (m³/m)	Annual ΔV_{lim} (m³/m/yr)	Annual ΔV_{unlim} (m³/m/yr)
Ref	62.9	73.8	16.5	19.3
Sc1	70.0	80.5	18.3	21.1
Sc2	68.3	73.8	17.9	19.3
Sc3	71.7	73.8	18.8	19.3
Sc4	72.1	73.8	18.9	19.3
Sc5	211.3	270.6	55.6	71.0
Sc6	61.2	70.6	16.1	18.6
Sc7	74.5	88.7	19.5	23.2

FIGURE 8 Fraction of time that supply to the foredune was limited (i.e., $q_{bdt,on} < q_{p,on}$) as a function of wind (a) speed U and (b) direction on the beach with respect to the shore normal θ_{SN}. The fractions were computed by binning all moments with non-zero $q_{p,on}$ in 1 m and 10° speed and direction bins, respectively. The values at the x-axes are the bin mids. Panel (b) also shows (black line) the 95% exceedance value of the water level at the shoreline, η_{sh}, for each direction bin [Color figure can be viewed at wileyonlinelibrary.com]

to an annual growth of about 19.3 m³/m ($r^2 = 0.98$; Table 2). From winter 2015–2016 onward, ΔV_{unlim} was persistently above the measured ΔV (Figure 7a). Of the moments with $q_{p,on} > 0$, 17.1% were predicted to be supply limited ($q_{bdt,on} < q_{p,on}$) because of fetch restrictions. Although this was 3.2% of the entire period only, the total supply-limited volume change ΔV_{lim} dropped below the unlimited growth and agreed better with the measured ΔV (Figure 7a). Only in 2018 was the growth in ΔV_{lim} less than in the observations; interestingly, this was also true for the growth in ΔV_{unlim}. In more detail, the supply limitations reduced the total ΔV_{lim} to about 85% of the total ΔV_{unlim} (62.9 m³/m; Table 2), and the best-fit linear line yielded 16.5 m³/m/yr ($r^2 = 0.98$; Table 2). This annual growth is almost exactly identical to the observed growth of 17.3 m³/m/yr. Consistent with the synthetic simulations presented previously, strong and onshore winds most commonly resulted in supply limitations (Figure 8). While conditions with local (on the beach) wind speeds smaller than 16 m/s were supply limited less than 35% in time; this percentage increased to over 65–75% for the highest wind speed encountered (Figure 8a). Onshore winds were supply limited up to 50% in time, while highly oblique to alongshore winds almost always caused transport rates at the beach–dune transition to equal potential rates because of very long fetches. The fraction distribution was, however, not symmetric around the shore-normal direction (Figure 8b). In contrast to southwesterly winds, winds from the northwest (positive θ_{SN}) often coincided with elevated water levels induced by a storm surge (Figure 8b). The associated smaller beach width and increased surface moisture values make supply limitations more common. The seasonality in the wind climate and TWL values (Figure 6c,e) explains why the cumulative (in time) difference between limited and unlimited foredune volume growth increased mainly in winter (Figure 2b). In the examined period,

this was particularly obvious in the 2016–2017 and 2018–2019 winters, but less so in the intermediate 2017–2018 winter.

3.2 | Scenario runs

Table 2 illustrates that the correction from regional to local wind data (Sc5) is by far the most influential factor in predicting foredune volume growth. Without correction, the annual $\Delta V_{unlim} = 71.0$ m³/m/yr was almost 3.7 times larger than in the reference run. As already pointed out by De Winter et al. (2020), the correction in wind speed is the dominant factor for the ΔV reduction in the reference run, with the more alongshore wind at the beach–dune transition being of secondary importance. Because the regional winds are stronger than the local winds, the critical fetches are larger and, accordingly, the mesoscale aeolian transport is relatively more supply limited. This is seen by the drop in the annual ΔV from 71.0 to 55.6 m³/m/yr (Table 2), an approximately 22% reduction compared to the 15% reduction in the reference run. Nonetheless, the annual ΔV_{lim} still exceeded the measured ΔV of 17.3 m³/m/yr by more than a factor of 3.

Without the limiting effects of rain on aeolian sand transport (Sc1), the limited and unlimited ΔV would have been about 7 m³/m larger during the total study period than in the reference run (Table 2). This equates to an 1.8 m³/m/yr difference, about 10% of the annual ΔV_{lim} without the rain effects. The results for scenarios 2 and 3 illustrate that surface moisture dynamics and beach width reductions by storm surges must also have contributed to the supply limitations in the reference run. With the beach width reductions and the transport commencing immediately at the shoreline rather than at the 10% moisture level (Sc2), the total ΔV_{lim} was substantially closer to the

total ΔV_{unlim} than in the reference run (68.3 m³/m, 92.5% of the total ΔV_{unlim}). Without the beach width reductions, the difference between the total limited and unlimited ΔV was even smaller (71.7 m³/m, 97.1% of the total ΔV_{unlim}). In this case, moisture dynamics is no longer of any major influence, as the results of Sc3 and Sc4 are almost exactly the same (Table 2). On the whole, the results of Sc1–Sc4 illustrate that rain as well as storm surges with their associated strong winds are the main conditions that cause meso-scale potential transport to overpredict measured foredune growth, at least at the present site and based on the adopted model formulations. In the latter condition, the surge-induced beach width reduction as well as the prolonged wet intertidal beach because of elevated groundwater levels both contribute to the predicted supply limitation.

As expected, ΔV predictions are also sensitive to the choice of the q_p equation. The Hsu (1971) equation including the U_* threshold of motion resulted in a slightly smaller annual ΔV_{lim} (16.1 compared to 16.5 m³/m/yr; Table 2), while the use of the Lettau and Lettau (1978) resulted in a somewhat larger value (19.5 compared to 16.5 m³/m/yr; Table 2). This sensitivity is slightly larger when compared to the limiting effects of rain, surface moisture and storm-surge-induced beach width variations (Sc1–Sc4), but of minor relevance compared to the topographic effects of the high and steep foredune on the regional wind speed and direction (Sc5).

3.3 | Frequency–magnitude analysis

Because the measured and limited dune volume growth agreed well, we can now examine during which wind characteristics most sand was transported onshore into the foredune during the study period.

To this end, a frequency–magnitude analysis (Wolman & Miller, 1960) was performed, in which all $q_{bdt,on}$ for moments with non-zero $q_{p,on}$ were binned corresponding to $U \pm 0.5$ m/s with the lowermost U bin mid at 8 m/s. Our frequency–magnitude analysis differs from Delgado-Fernandez and Davidson-Arnott's (2011) approach in the sense that they defined transport events and hence included event duration as an additional variable in their analysis. We return to this difference below. As expected, the frequency of non-zero transport moments decreased with U (Figure 9a). On the whole, the bin-median onshore transport rate at the beach–dune transition increased only weakly with U (Figure 9b) and was always well below the maximum possible transport rate (i.e., q_p for shore-normal wind). For the lower wind speeds this was primarily due to the cosine effect (Equation 6), while for higher wind speeds also supply limitations played a substantial role (Figure 8a); the zero transport in the bin with mid $U = 22$ m/s reflects the latter clearly. Figure 9c illustrates that the predicted limited foredune volume growth was due neither to the most frequent wind speeds just above the threshold nor to the highest wind speeds ($U > 15.5$ m/s contributed less than 4% to the predicted ΔV_{lim}), but to more moderate wind speeds between 9.5 and 12.5 m/s. These winds were fairly common (Figure 9a) and mostly did not coincide with supply limitations (Figure 8a). These results reaffirm earlier suggestions (Arens, 1996; Davidson-Arnott, 1990; Delgado-Fernandez & Davidson-Arnott, 2011) about the importance of moderate rather than extreme wind speeds to meso-scale foredune growth. Interestingly, also the predicted unlimited foredune growth was in our dataset dominated by these moderate wind speeds (not shown). The magnification of the transport rates at the largest U without supply limitations are still completely outweighed by the associated very low frequency of occurrence. This finding should not be interpreted as
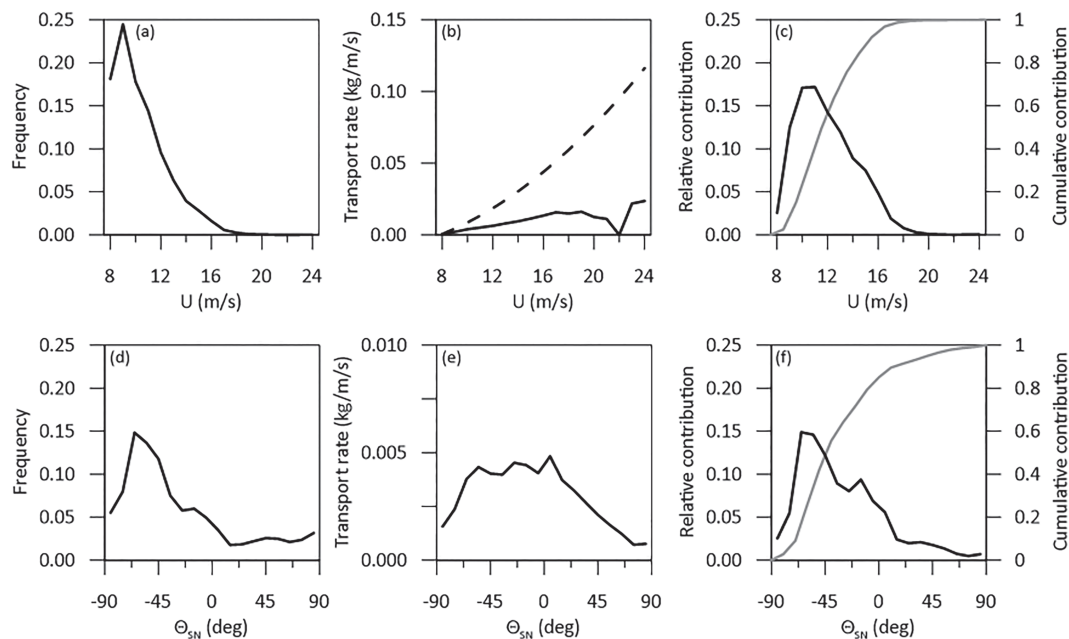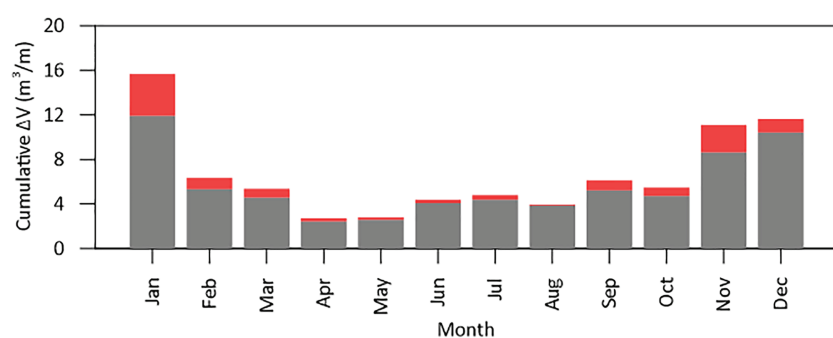

FIGURE 9 Frequency–magnitude analysis of reference run: (a) frequency of occurrence of wind speed U; (b) transport magnitude q; and (c) relative (black line) and cumulative (grey line) contribution of U to the predicted foredune growth ΔV_{lim} during the study period. The results in parts (a)–(c) are based on wind speed bins with a width of 1 m/s, with the first bin mid at 8 m/s. The dashed line in part (b) is the transport magnitude in the case of a shore-normal wind and no supply limitations. Parts (d)–(f) show the frequency–magnitude analysis for the wind direction with respect to the shore-normal, θ_{SN}. The wind direction bin width in (d)–(f) is 10°, with the first bin mid at 85°. Negative and positive θ_{SN} are from southern and northern directions, respectively

that the entire event with these very large winds does not contribute to potential foredune growth. A very-large-magnitude wind event generally has a long duration, and may account for a considerable part of the potential annual growth (Delgado-Fernandez & Davidson-Arnott, 2011); however, our binning approach suggests that the peak moment of the event itself contributes little.

A frequency–magnitude analysis was also performed by binning the same moments in directional bins with a width of 10° from (bin mids) $\theta_{SN} = -85$ to $+85°$. Consistent with the long-term wind climate (e.g., Ruessink et al., 2018), highly oblique winds from the southwest were most common during the study period (Figure 9d), with the mode at $\theta_{SN} = -65°$. The bin-median transport magnitude clearly reflects the cosine effect, with the smallest transport rates for near-alongshore winds ($\theta_{SN} = \pm 85°$) and the largest for shore-normal winds (Figure 9e), although rather large bin-averaged transport rates were also found for southwesterly winds ($\theta_{SN} = -45°$). As a consequence, the meso-scale foredune growth at the present site is predicted to be dominated by southwesterly winds (Figure 9f), with the mode at $\theta_{SN} = -65°$. These winds were the most frequent and were associated with large (mean) transport rates, also because of minimal supply limitations (Figure 8b). Winds from the northwest (positive θ_{SN}) contributed only 10% to ΔV_{lim}. To summarize, the foredune growth at the Egmond study site is predicted to be dominated by moderately strong (9.5–12.5 m/s), highly oblique (southwesterly) winds; these are both common and do not result in major supply limitations.

3.4 | Monthly timescales

To examine which month contributed most to the measured meso-scale foredune growth, the predictions of the reference run were extended to include the period from 7 January to 15 March 2015 in order to have an exactly 4-year-long study period; each calendar month is thus included exactly four times. Although the differences between limited and unlimited foredune growth were largest in January, November and December (Figure 10; see also Figure 7b), the foredune growth in these months was still predicted to be largest with a combined 45% contribution to the ΔV_{lim} growth in the entire 4-year period. Consistent with the monthly wind climate (Figure 6c), the foredune grew least in the months April to August, even though supply limitations in these months were minimal (ratio of limited to unlimited $\Delta V > 0.9$, compared to ≈ 0.75 in November and February). Psamathe thus predicted a clear seasonal variation in foredune growth, with largest growth in winter, even though the seasonality is somewhat suppressed by a coinciding seasonality in supply limitation.

4 | DISCUSSION

Meso-scale aeolian sand supply to foredunes was predicted by expanding an earlier proposed equation (Bauer & Davidson-Arnott, 2003) to predict the downwind increase in aeolian transport over a beach profile with spatially varying surface moisture content, including a pragmatic equation (Delgado-Fernandez, 2011) to relate this variable moisture content to the critical fetch. Model parameters in the groundwater module were set to values based on an earlier $\eta(x,t)$ data model comparison, while those in the retention curve and in the computation of the wind shear velocity were derived from previous field observations. Literature values were used for all other parameters; in other words, none were used to optimize the prediction of foredune volume growth. The good agreement between measured and modelled ΔV suggests that the chosen approach is a viable means to bridge the scale gap between short-term aeolian process dynamics with all its inherent complexity to meso-scale foredune volume growth. Despite the low fraction of time that aeolian supply on Egmond beach was predicted to be limited, the meso-scale effect of these limitations was substantial (Figures 7 and 10). In 2018 the predicted foredune growth was less than in the observations, even without supply limitations (Figure 7a). Wind data collected at Egmond illustrate a substantial effect of the embryo dune ridge on the local wind speeds, especially for shore-oblique to alongshore winds (De Winter et al., 2020). Because the ridge became higher and wider during the study period (Ruessink et al., 2019) it may be that in 2018 sand blown into the study area from alongshore (where there are no embryo dunes) deposited on the ridge because of the ridge-induced reduction in wind speed. In the model, alongshore wind obviously does not contribute to foredune volume growth. In future studies, the generality of these findings must be addressed by applying the model to sites with other beach widths, grain sizes as well as wind, tide and wave forcing. It would also be worthwhile exploring how factors that we have ignored could be included in the model, such as the effect of evaporation and condensation on surface moisture dynamics (Schmutz & Namikas, 2018), the influence of sediment sorting on the aeolian transport rate (Van Rijn & Strypsteen, 2020), the dependence of the roughness length z_0 and hence the ratio of U_* to U on grain size and surface texture (Sherman & Farrell, 2008), and the downwind change in wind speed over the beach (De Winter et al., 2020). The last two factors point to the more complicated character of wind flow over beach surfaces than assumed in Psamathe.

All simulations were run with a single time-independent and monotonically upward-sloping cross-shore profile, and it is possible that its shape may have affected the results. First, the low (1:50) slope

FIGURE 10 Cumulative foredune growth ΔV versus calendar month based on the predictions from 7 January 2015 to 7 January 2019 with the same model settings as in the reference run. The period is slightly larger than in the reference run, and the total ΔV_{lim} is thus also larger (68.0 m^3/m versus 62.9 m^3/m in Figure 7). The dark-grey bars are the cumulative ΔV_{lim} and the red bars represent the cumulative supply limitation. The sum of the grey and red bars is thus the cumulative ΔV_{unlim} in each month [Color figure can be viewed at wileyonlinelibrary.com]

in combination with $w_{s,max} = 10\%$ caused most of the intertidal zone to remain too wet for aeolian transport. During the study period, the lowest z with non-zero q in Equation (4) was near 0.6 m MSL, which is just below the mean high-tide level (≈ 0.85 MSL). Multi-year video imagery collected at Egmond show the most pronounced visual signatures of aeolian transport, in the form of aeolian bedforms known as sand strips, on the upper intertidal and dry beach (Duarte-Campos et al., 2018; Hage et al., 2018), qualitatively consistent with the model results. On the other hand, Swann et al. (2021) recently observed substantial non-zero aeolian transport over a wet ($w_s = 16 - 17\%$) intertidal beach. This suggests that Psamathe may have underestimated the importance of the low-sloping intertidal zone as an aeolian sand source for foredune growth. Secondly, our simulations may have missed the potential effect of temporal sandbar variability on aeolian processes (Houser, 2009). Observations at the study site have shown that the moisture content of the sand at the crest of a well-developed intertidal sandbar can become sufficiently small (Smit et al., 2019; Tuijman et al., 2020) to enable aeolian transport when the wind is strong and highly shore-oblique to alongshore directed (Hage et al., 2018). The landward trough usually remains saturated (Smit et al., 2019) and therefore disconnects the aeolian transport systems on the bar and the upper beach (see also Oblinger & Anthony, 2008), suggesting the importance of wind-blown intertidal sand to foredune growth to be low. Wind-blown sand may be transferred from the intertidal to the upper beach and foredune after the onshore welding of the bar and the associated disappearance of the trough (Houser, 2009). At the study site this mostly takes place in summer after prolonged periods of quiescent conditions (Masselink et al., 2006; Quartel et al., 2007). Then, fetch restrictions are already rare (Figure 8) and meso-scale supply to the foredune is low (Figure 10). On the whole, we therefore argue that the use of a static profile without an intertidal sandbar was not a serious shortcoming in our simulations. Future work is necessary to thoroughly test the validity of our arguments and to examine its applicability at other sites, especially those where seasonal and interannual variations in beach width are much more pronounced (e.g., Davidson-Arnott & Law, 1996) than at our study site.

Finally, we stress that the good agreement between the supply-limited and measured foredune volume growth relied heavily on the correction of the regional wind speed and direction to beach values. Without this correction (Sc5), agreement was poor, even with supply limitations (Table 2). It is unlikely that the data-based wind correction values (Tuijman et al., 2020) used here are generally applicable, as they are likely to depend on foredune characteristics, such as height and slope, and on the location of the regional meteorological station (see also Rotnicka & Dłużeski, 2019). Had that station been on land, for example, the correction factors for the wind speed might have been above 1, given the reduction in wind speed over land because of the rough terrain. In line with De Winter et al. (2020), we suggest the use of computational fluid dynamics (CFD) (Hesp & Smyth, 2021; Smyth, 2016) to transform regional to local wind data in case local wind observations are not available. Multiple CFD runs could be used to construct a lookup table with correction values for the foredune at the site under study. A first CFD application for our study site to compute such a table (Donker et al., 2018) showed promising results in comparison to the data-based values applied here. The extension of this preliminary study to sites with different foredune characteristics is highly desirable.

5 | CONCLUSIONS

We have expanded the fetch model for the meso-scale (seasons to years) modelling of aeolian sand transport across the beach–dune transition into a quantitative framework by coupling existing groundwater and surface moisture modules to a fetch module that predicts the downwind increase in aeolian sand transport over a beach with spatially varying surface moisture. The proposed model was applied to an almost 4-year-long dataset of foredune evolution at Egmond, The Netherlands. With model parameters taken from the existing literature and a data-based correction of the regional wind forcing for the topographic effects of the high and steep foredune at the site, the model performance was highly satisfactory. The predicted annual foredune growth of 16.5 m^3/m/yr compared very favourably to the observed growth of 17.3 m^3/m/yr. Although the vast majority of transport moments resulted in the maximum possible aeolian supply at the beach–dune transition, the few cases with supply limitations reduced foredune growth by about 2.8 m^3/m annually. These moments were characterized by strong (mostly above 16 m/s) and onshore winds, or by shore-oblique winds that were associated with a substantial rise in water level and hence a wetter and narrower beach. Rain was also predicted to limit foredune growth (about 1.8 m^3/m/yr). Consistent with suggestions in the literature, fairly common shore-oblique winds with moderate speeds (9.5–12.5 m/s) rather than extreme but very infrequent winds contributed most to the observed meso-scale foredune growth. As these conditions at the study site were most common in winter, the model also predicted substantial seasonal variation in foredune growth, consistent with the observations. Additional validations with meso-scale datasets are required to thoroughly test the generality of our findings and to determine the model's applicability in other environmental settings.

CONFLICT OF INTEREST

The authors declare no conflict of interest.

DATA AVAILABILITY STATEMENT

The model code, developed in MATLAB, is available from https://github.com/UtrechtCoastalGroup/Psamathe. The Egmond dataset is available from the Zenodo repository https://doi.org/10.5281/zenodo.2635416.

ORCID

Gerben Ruessink https://orcid.org/0000-0001-9526-6087

Geert Sterk https://orcid.org/0000-0002-3304-7249

Yvonne Smit https://orcid.org/0000-0002-9770-237X

Winnie De Winter https://orcid.org/0000-0002-2333-5650

Pam Hage https://orcid.org/0000-0002-9218-6855

Jasper J. A. Donker https://orcid.org/0000-0003-2465-057X

Sebastiaan M. Arens https://orcid.org/0000-0001-8680-5755

REFERENCES

Arens S.M. (1996) Rates of aeolian transport on a beach in a temperate humid climate. *Geomorphology*, 17, 3–18.

Arens S.M. (1997) Transport rates and volume changes in a coastal foredune on a Dutch Wadden island. *Journal of Coastal Conservation*, 3, 49–56.

Barbier E.B., Hackers S.D., Kennedy C., Koch E.W., Stier A.C., Silliman B.R. (2011) The value of estuarine and coastal ecosystem services. *Ecological Monographs*, 81(2), 169–183.

Bauer B.O., Davidson-Arnott R. G. D. (2003) A general framework for modeling sediment supply to coastal dunes including wind angle, beach geometry, and fetch effects. *Geomorphology*, 49, 89–108.

Bauer B.O., Davidson-Arnott R. G. D., Hesp P.A., Namikas S.L., Ollerhead J., Walker I. (2009) Aeolian sediment transport on a beach: surface moisture, wind fetch, and mean transport. *Geomorphology*, 105, 106–116.

Bauer B.O., Davidson-Arnott R. G. D., Walker I.J., Hesp P.A., Ollerhead J. (2012) Wind direction and complex sediment transport response across a beach–dune system. *Earth Surface Processes and Landforms*, 37, 1661–1677.

Brakenhoff L.B., Smit Y., Donker J. J. A., Ruessink G. (2019) Tide-induced variability in beach surface moisture: observations and modelling. *Earth Surface Processes and Landforms*, 44, 317–330. https://doi.org/10.1002/esp.4493

Bullard J.E., Ackerley D., Millett J., Chandler J.H., Montreuil A.L. (2019) Post-storm geomorphic recovery and resilience of a prograding coastal dune system. *Environmental Research Communications*, 1, 13. https://doi.org/10.1088/2515-7620/ab0258

Castelle B., Marieu V., Bujan S., Splinter K.D., Robinet A., Sénéchal N. et al. (2015) Impact of the winter 2013–2014 series of severe Western Europe storms on a double-barred sandy coast: beach and dune erosion and megacusp embayments. *Geomorphology*, 2015, 135–148.

Castelle B., Bujan S., Ferreira S., Dodet G. (2017) Foredune morphological changes and beach recovery from the extreme 2013/2014 winter at a high-energy sandy coast. *Marine Geology*, 385, 41–55.

Cohn N., Ruggiero P., De Vries S., Kaminsky G.M. (2018) New insights on coastal foredune growth: the relative contributions of marine and aeolian processes. *Geophysical Research Letters*, 45, 4965–4973. https://doi.org/10.1029/2018GL077836

Cohn N., Hoonhout B.M., Goldstein E.B., De Vries S., Moore L.J., Durán Vinent O. et al. (2019) Exploring marine and aeolian controls on coastal foredune growth using a coupled numerical model. *Journal of Marine Science and Engineering*, 7, 13. https://doi.org/10.3390/jmse7010013

Davidson S.G., Hesp P.A., Miot da Silva G. (2020) Controls on dune scarping. *Progress in Physical Geography*, 44, 923–947. https://doi.org/10.1177/0309133320932880

Davidson-Arnott R. G. D. (1990) Seasonal patterns and controls on sediment supply to coastal foredunes, Long Point, Lake Erie. In *Coastal dunes: form and process*, Wiley: Chichester; 177–200.

Davidson-Arnott R. G. D., Dawson J.C. (2001) Moisture and fetch effects on rates of aeolian sediment transport, Skallingen, Denmark, Canadian Coastal Conference, 2001.

Davidson-Arnott R. G. D., Law M.N. (1996) Measurement and prediction of long-term sediment supply to coastal foredunes. *Journal of Coastal Research*, 12, 654–663.

Davidson-Arnott R. G. D., Yang Y., Ollerhead J., Hesp P.A., Walker I.J. (2008) The effects of surface moisture on aeolian sediment transport threshold and mass flux on a beach. *Earth Surface Processes and Landforms*, 33, 55–74.

De Vries S., Southgate H.N., Kanning W., Ranasinghe R. (2012) Dune behavior and aeolian transport on decadal timescales. *Coastal Engineering*, 67, 41–53.

De Winter R. C., Ruessink B.G. (2017) Sensitivity analysis of climate change impacts on dune erosion: case study for the Dutch Holland coast. *Climatic Change*, 141, 685–701. https://doi.org/10.1007/s10584-017-1922-3

De Winter R. C., Gongriep F., Ruessink B.G. (2015) Observations and modeling of alongshore variability in dune erosion at Egmond aan Zee, the Netherlands. *Coastal Engineering*, 99, 167–175.

De Winter W., Donker J., Sterk G., Van Beem J., Ruessink G. (2020) Regional versus local wind speed and direction at a narrow beach with a high and steep foredune. *PLOS ONE*, 15(1), e0226983. https://doi.org/10.1371/journal.pone.0226983

Delgado-Fernandez I. (2010) A review of the application of the fetch effect to modelling sand supply to coastal foredunes. *Aeolian Research*, 2, 61–70.

Delgado-Fernandez I. (2011) Meso-scale modelling of aeolian sediment input to coastal dunes. *Geomorphology*, 130, 230–243.

Delgado-Fernandez I., Davidson-Arnott R. (2011) Meso-scale aeolian sediment input to coastal dunes: the nature of aeolian transport events. *Geomorphology*, 126, 217–232.

Di Cosmo R., Maurao J., Zacchiroli S., Zavattaro G. (2014) Aeolus: a component model for the cloud. *Information and computation*, 239, 100–121. https://doi.org/10.1016/j.ic.2014.11.002

Donker J., De Winter W., Ruessink G. (2018) Modelling the effect of coastal foredune topography on annual aeolian sand input from the beach. *Geophysical Research Abstracts*: 8748. https://meetingorganizer.copernicus.org/EGU2018/EGU2018-8748-1.pdf

Duarte-Campos L., Wijnberg K.M., Hulscher S. J. M. H. (2018) Estimating annual onshore aeolian sand supply from the intertidal beach using an aggregated-scale transport formula. *Journal of Marine Science and Engineering*, 6(127), 22. https://doi.org/10.3390/jmse6040127

Durán O., Claudin P., Andreotti B. (2011) On aeolian transport: grain-scale interactions, dynamical mechanisms and scaling laws. *Aeolian Research*, 3(3), 243–270. https://doi.org/10.1016/j.aeolia.2011.07.006

Ellis J.T., Sherman D.J. (2013) Fundamentals of aeolian sediment transport: wind-blown sand. In *Treatise on Geomorphology*, Shroder J. F. (ed), Vol. 11, Elsevier: Amsterdam; 85–108.

Everard M., Jones L., Watts B. (2010) Have we neglected the societal importance of sand dunes? An ecosystem services perspective. *Aquatic Conservation: Marine and Freshwater Ecosystems*, 20, 476–487.

Gillette D.A., Herbert G., Stockton P.H., Owen P.R. (1996) Causes of the fetch effect in wind erosion. *Earth Surface Processes and Landforms*, 21, 641–659.

Hage P.M., Ruessink B.G., Donker J. J. A. (2018) Determining sand strip characteristics using argus video monitoring. *Aeolian Research*, 33, 1–11. https://doi.org/10.1016/j.aeolia.2018.03.007

Hage P.M., Ruessink G., Van Aartrijk Z., Donker J. (2020) Using video monitoring to test a fetch-based aeolian sand transport model. *Journal of Marine Science and Engineering* 8(2). https://doi.org/10.3390/jmse8020110

Hallin C., Larson M., Hanson H. (2019) Simulating beach and dune evolution at decadal to centennial scale user rising sea levels. *PLoS ONE*, 14, e0215651. https://doi.org/10.1371/journal.pone.0215651

Hesp P.A., Smyth T. A. G. (2021) CFD flow dynamics over model scarps and slopes. *Physical Geography*, 42(1), 1–24. https://doi.org/10.1080/02723646.2019.1706215

Houser C. (2009) Synchronization of transport and supply in beach–dune interaction. *Progress in Physical Geography*, 33, 733–746.

Houser C., Ellis J. (2013) Beach and dune interaction. In *Treatise on geomorphology*, Shroder J. F. (ed), Academic Press: San Diego, CA; 267–288.

Hsu S.A. (1971) Wind stress criteria in eolian sand transport. *Journal of Geophysical Research*, 76, 8684–8686.

Hsu S.A. (1974) Computing eolian sand transport from routine weather data, Proceedings of 14th Conference on Coastal Engineering.

Iversen J.D., Rasmussen K.R. (1994) The effect of surface slope on saltation threshold. *Sedimentology*, 41, 721–728.

Jackson D. W. T., Cooper J. A. G. (1999) Beach fetch distance and aeolian sediment transport. *Sedimentology*, 46, 517–522.

Kang H.Y., Nielsen P., Hanslow D.J. (1994) Watertable overheight due to wave runup on a sandy beach, Proceedings of the 24th International Conference on Coastal Engineering.

Keijsers J. G. S., Poortinga A., Riksen M. J. P. M., Maroulis J. (2014) Spatio-temporal variability in accretion and erosion of coastal foredunes in the Netherlands: regional climate and local topography. *PLOS ONE*, 9, e91115. https://doi.org/10.1371/journal.pone.0091115

Kok J.F., Partell E. J. R., Michaels T.I., Karam D.B. (2012) The physics of wind-blown sand and dust. *Reports on Progress in Physics*, 75, 72.

Lettau K., Lettau H. (1978) Experimental and micrometeorological field studies of dune migration: IES report. In *Exploring the world's driest climate*, Lettau H. H., Lettau K. (eds), Vol. 101, Center for Climatic Research: University of Wisconsin–Madison; 110–147.

Luijendijk A., Hagenaars G., Ranasinghe R., Baart F., Donchyts G., Aarninkhof S.. 2018. The state of the world's beaches. *Scientific Reports* 8(664): 1–11. https://doi.org/10.1038/s41598-018-24630-6

Masselink G., Kroon A., Davidson-Arnott R. G. D. (2006) Morphodynamics of intertidal bars in wave-dominated coastal settings: a review. *Geomorphology*, 73, 33–49.

Morton R.A., Paine J.G., Gibeaut J.C. (1994) Stages and durations of post-storm beach recovery, Southeastern Texas Coast USA. *Journal of Coastal Research*, 10, 884–908.

Namikas S.L., Edwards B.L., Bitton M. C. A., Booth J.L., Zhu Y. (2010) Temporal and spatial variabilities in the surface moisture content of a fine-grained beach. *Geomorphology*, 114, 303–310. https://doi.org/10.1016/j.geomorph.2009.07.011

Oblinger A., Anthony E.J. (2008) Surface moisture variation on a multi-barred macrotidal beach: implications for aeolian sand transport. *Journal of Coastal Research*, 24, 1194–1199.

Plant N.G., Holland K.T., Puleo J.A. (2002) Analysis of the scale of errors in nearshore bathymetric data. *Marine Geology*, 191, 71–86.

Pollock L.W., Hummon W.D. (1971) Cyclic changes in interstitial water content, atmospheric exposure, temperature in a marine beach. *Limnology and Oceanography*, 16, 522–535.

Quartel S., Ruessink B.G., Kroon A. (2007) Daily to seasonal cross-shore behaviour of quasi-persistent intertidal beach morphology. *Earth Surface Processes and Landforms*, 32, 1293–1307.

Quartel S., Kroon A., Ruessink B.G. (2008) Seasonal accretion and erosion patterns of a microtidal sandy beach. *Marine Geology*, 250, 19–33.

Raubenheimer B., Guza R.T., Elgar S. (1999) Tidal water table fluctuations in a sandy ocean beach. *Water Resources Research*, 35, 2313–2320.

Roelvink D., Reniers A., van Dongeren A., van Thiel de Vries J., McCall R., Lescinski J. (2009) Modelling storm impacts on beaches, dunes and barrier islands. *Coastal Engineering*, 56, 1133–1152.

Rotnicka J., Dłużeski M. (2019) A method to derive long-term coastal wind data from distant weather station to improve aeolian sand transport rate prediction. *Aeolian Research*, 38, 24–38.

Ruessink B.G., Arens S.M., Kuipers M., Donker J. J. A. (2018) Coastal dune dynamics in response to excavated foredune notches. *Aeolian Research*, 31, 3–17.

Ruessink G., Schwarz C.S., Price T.D., Donker J. J. A. (2019) A multi-year data set of beach–foredune topography and environmental forcing conditions at Egmond aan Zee, The Netherlands. https://doi.org/10.3390/data4020073

Sarre R.D. (1989) Aeolian sand drift from the intertidal zone on a temper-ate beach: potential and actual rates. *Earth Surface Processes and Landforms*, 14, 247–258.

Schmutz P.P., Namikas S.L. (2018) Measurement and modeling of the spa-tiotemporal dynamics of beach surface moisture content. *Aeolian Research*, 34, 35–48.

Schwarz C., Van Starrenburg C., Donker J., Ruessink G. (2021) Wind and sand transport across a vegetated foredune slope. *Journal of Geo-physical Research: Earth Surface*, 125(e2020JF005732), 18. https://doi.org/10.1029/2020JF005732

Shao Y.P., Lu H. (2000) A simple expression for wind erosion threshold friction velocity. *Journal of Geophysical Research*, 105, 22437–22443.

Shao Y., Raupach M.R. (1992) The overshoot and equilibrium of saltation. *Journal of Geophysical Research*, 97, 20,559–20,564.

Sherman D.J. (1995) Problems of scale in the modelling and interpretation of coastal dunes. *Marine Geology*, 124, 339–349.

Sherman D. & Farrell E.J. (2008) Aerodynamic roughness lengths over movable beds: comparison of wind tunnel and field data. https://doi.org/10.1029/2007JF000784

Smit Y. (2019) Surface moisture dynamics on a narrow beach. PhD thesis, Utrecht University.

Smit Y., Donker J. J. A., Ruessink G. (2019) Spatiotemporal surface moisture variations on a barred beach and their relationship with groundwater fluctuations. *Hydrology*, 6, 8. https://doi.org/10.3390/hydrology6010008

Smyth T. A. G. (2016) A review of computational fluid dynamics (CFD) air-flow modelling over aeolian landforms. *Aeolian Research*, 22, 153–164.

Stockdon H.F., Holman R.A., Howd P.A., Sallenger Jr A.H. (2006) Empirical parameterization of setup, swash and runup. *Coastal Engineering*, 53, 573–588. https://doi.org/10.1016/j.coastaleng.2005.12.005

Strypsteen G., Houthuys R., Rauwoens P. (2019) Dune volume changes at decadal timescales and its relation with potential aeolian transport. *Journal of Marine Science and Engineering*, 7(357), 24. https://doi.org/10.3390/jmse7100357

Swann C., Lee D., Trimble S., Key C. (2021) Aeolian sand transport over a wet, sandy beach. *Aeolian Research*, 51, 100712. https://doi.org/10.1016/j.aeolia.2021.100712

Tuijman J.T., Donker J. J. A., Schwarz C.S., Ruessink G. (2020) Conse-quences of a storm surge for aeolian sand transport on a low-gradient beach. *Journal of Marine Science and Engineering*, 8, 2. https://doi.org/10.3390/jmse8080584

Tuller M., Or D. (2005) Water retention and characteristic curve. In *Encyclope-dia of soils in the environment*, Hillel D. (ed), Elsevier: Oxford; 278–289.

Van Dijk P. M., Arens S.M., van Boxel J. H. (1999) Aeolian processes across transverse dunes. II. Modelling the sediment transport and profile development. *Earth Surface Processes and Landforms*, 24, 319–333.

Van Gent M. R. A., Van Thiel de Vries J. S. M., Coeveld E.M., De Vroeg J., Van de Graaff J. (2008) Large-scale dune erosion tests to study the influence of wave periods. *Coastal Engineering*, 55(12), 1041–1051.

Van Genuchten M. T. (1980) A closed-form equation for predicting the hydraulic conductivity of unsaturated soils. *Soil Science Society of America Journal*, 44, 892–898.

Van Rijn L. C., Strypsteen G. (2020) A fully predictive model for aeolian sand transport. *Coastal Engineering*, 156(103600), 19. https://doi.org/10.1016/j.coastaleng.2019.103600

Van Thiel de Vries J. S. M., van Gent M. R. A., Walstra D. J. R., Reniers A. J. H. M. (2008) Analysis of dune erosion processes in large-scale flume experiments. *Coastal Engineering*, 55, 1028–1040.

Walker I.J., Davidson-Arnott R. G. D., Bauer B.O., Hesp P.A., Delgado-Fernandez I., Ollerhead J., Smyth T. A. G.. 2017. Scale-dependent perspectives on the geomorphology and evolution of beach-dune systems. *Earth-Science Reviews* 171: 220–253.

Wijnberg K.M. (2002) Environmental controls on the decadal morphologic behaviour of the Holland coast. *Marine Geology*, 189, 227–247.

Wolman M.G., Miller J.P. (1960) Magnitude and frequency of forces in geomorphic processes. *Journal of Geology*, 68, 54–74.

Yokobori M., Kuriyama Y., Shimozono T., Tajima Y. (2020) Numerical simu-lation of volume change on the backshore induced by cross-shore aeolian sediment transport. *Journal of Marine Science and Engineering*, 8, 438. https://doi.org/10.3390/jmse8060438